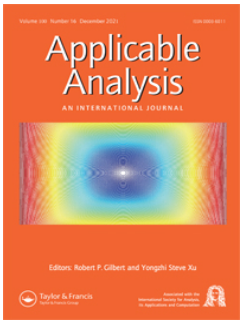

Taylor & Francis
Taylor & Francis Group

Applicable Analysis
An International Journal

ISSN: (Print) (Online) Journal homepage: https://www.tandfonline.com/loi/gapa20

Modelling virus contact mechanics under atomic force imaging conditions

Paolo Piersanti, Kristen White, Bogdan Dragnea & Roger Temam

To cite this article: Paolo Piersanti, Kristen White, Bogdan Dragnea & Roger Temam (2022): Modelling virus contact mechanics under atomic force imaging conditions, Applicable Analysis, DOI: 10.1080/00036811.2022.2044027

To link to this article: https://doi.org/10.1080/00036811.2022.2044027

Published online: 26 Feb 2022.

APPLICABLE ANALYSIS
https://doi.org/10.1080/00036811.2022.2044027

Taylor & Francis
Taylor & Francis Group

Modelling virus contact mechanics under atomic force imaging conditions

Paolo Piersanti[a], Kristen White[b], Bogdan Dragnea[b] and Roger Temam[a]

[a]Department of Mathematics and Institute for Scientific Computing and Applied Mathematics, Indiana University Bloomington, Bloomington, IN, USA; [b]Department of Chemistry, Indiana University Bloomington, Bloomington, IN, USA

ABSTRACT

In this paper, we present a discrete model governing the deformation of a convex regular polygon subjected not to cross a given flat rigid surface, on which it initially lies in correspondence of one point only. First, we set up the model in the form of a set of variational inequalities posed over a non-empty, closed and convex subset of a suitable Euclidean space. Second, we show the existence and uniqueness of the solution. The model provides a simplified illustration of processes involved in virus imaging by atomic force microscopy: adhesion to a surface, distributed strain, relaxation to a shape that balances adhesion and elastic forces. The analysis of numerical simulations results based on this model opens a new way of estimating the contact area and elastic parameters in virus contact mechanics studies.

ARTICLE HISTORY
Received 21 December 2021
Accepted 10 February 2022

COMMUNICATED BY
Y. S. Xu

KEYWORDS
Elliptic variational inequalities; contact mechanics; biological systems

2020 MATHEMATICS SUBJECT CLASSIFICATIONS
74M15; 35Q92; 35J86; 92B05

1. Introduction

Due to its relevance for a variety of natural phenomena, contact mechanics of nanoscopic, isometric polyhedral shells is a topic of great interest. For instance, the formation of polyhedral cages of water molecules encapsulating other chemical species at low temperatures and high pressures govern the sequestration of hydrocarbon gas molecules on arctic sea floors and in permafrost [1]. Bulk polycrystalline samples of such gas hydrates (clathrates) can be 20–40 times stronger than ice under uniaxial compression. At larger spatial scales, but still nanoscopic, highly symmetric virus protein cages encapsulate nucleic acid cargo, exhibiting a hardness that is responsive to the chemical environment. For such examples the discrete nature of the subunits and the size dependence of their properties cannot be ignored when attempting to understand cage mechanics in response to chemical or physical forces.

During the virus life cycle, there are multiple instances of interactions with interfaces. The ensuing mechanical stresses elicit a response from either the host or the virus [2]. Since the nature and magnitude of resultant deformations are key to understanding the response, virus mechanics has been the topic of both experimental and computational studies [3–5]. In many viruses, the attractive interactions between the protein building blocks of a virus shell (also known as the capsid) are necessarily weak, at least at the assembly stage [6, 7]. This allows for error correction, during the growth phase. By comparison, the oligomeric building blocks themselves tend to be much more stable against dissociation [8, 9]. As a consequence of the difference in intra- and inter-subunit interaction

CONTACT Roger Temam temam@indiana.edu
This article is dedicated to Robert P. Gilbert on the occasion of his 90th birthday, with friendship and much appreciation for his scientific contributions and for his services to the community.

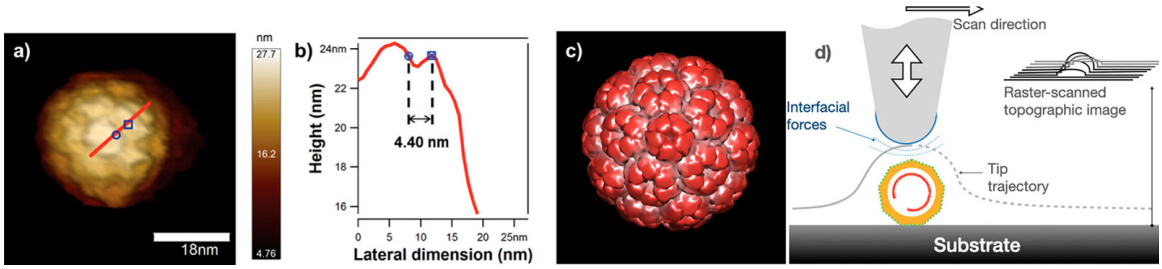

Figure 1. (a) Example of an AFM image of a Brome Mosaic Virus (BMV) particle in aqueous medium. (b) Cross-section showing the shape profile and typical attainable resolution. (c) Molecular model (reprinted with permission from Ref. [4]). (d) Schematic of the atomic force probe-sample geometry. The probe is in the shape of a rounded, inverted cone (gray). The sample is formed of a virus (orange) adsorbed on the surface of a flat, solid substrate. As the probe tip is laterally scanned over the substrate, the probe-sample distance is kept constant, and the tip trajectory relative to a reference position is recorded.

potential energies, and of the geometric frustration, local strain is expected to vary across the shell structure [10, 11]. The inhomogeneous elastic stress distribution will influence how capsids deform under mechanical stress.

Early theories of mechanical deformation in viruses sought to explain observations from nanoindentation experiments [12, 13]. Nanoindentation experiments involve the measurement of axial compression as a function of the force exerted by an atomic force microscope (AFM) probe in a direction normal to the substrate on which the virus sits [14, 15]. Early models were based on the continuum theory of elasticity [16, 17]. Later on, the discrete nature of the building blocks was taken into account in coarse-grained and all-atom molecular dynamics models of nanoindentation [18–21]. These models provided better qualitative predictions for stiffness distribution across the capsid than the continuum theory, at least for small viruses. They are also inherently capable of including fluctuations, which can influence the path through the energy landscape as the virus is deformed. However, the great complexity of some of the numerical models makes it difficult to differentiate the layers that would lead to a conceptual understanding of the process. The challenges are even greater if one considers that, in nanoindentation experiments, the read-out of a three-dimensional conformational change is one-dimensional (axial distance). Solving the inverse problem of finding material mechanical parameters from the axial distance dependence depends on the model. Moreover, since the exact AFM probe-virus contact geometry changes from particle to particle and probe to probe, force–deformation curves usually show significant experimental spread.

In this paper, we propose a new way to perform a three-dimensional measurement of conformational changes of a virus under directional pressure and extract elastic parameters via an elastic model based on a system of coupled discrete subunits with localized interactions. The model we will be considering is discrete and is governed by a set of variational inequalities posed over a nonempty, closed and convex subset of the Euclidean space. Similar problems have been considered in the continuum framework in the static case [22–27] and in the time-dependent case [28]. For clarity and simplicity, we consider the geometry two-dimensional, and the interactions linear. Extensions to three dimensions and non-linear interactions will be considered in the forthcoming paper [29].

2. Basic principles of atomic force microscopy

Atomic force microscopy (AFM) is currently the only method capable of imaging small virus morphology in real-time under environmental conditions, with a spatial resolution routinely reaching 3–5 nm [4, 30–33]. The study of single virus particles by atomic force microscopy and force spectroscopy has led to insights in virus mechanics and its relationship between the virus structure and the chemical environment [3, 5, 34–38]. A schematic of the atomic force imaging principle is presented in Figure 1.

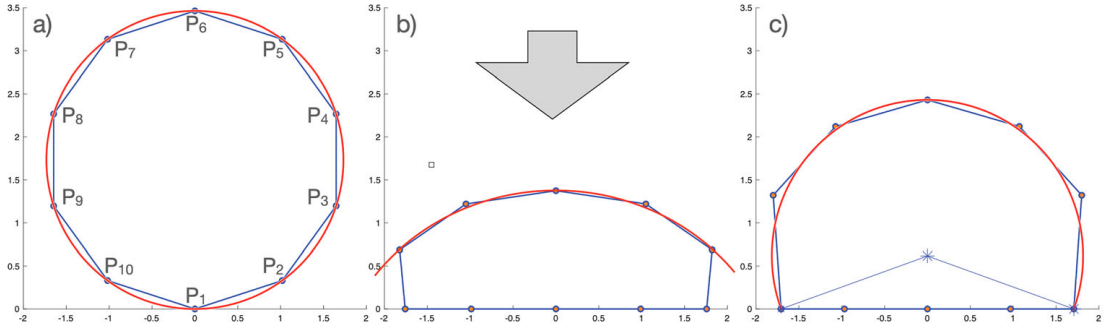

Figure 2. (a) A convex regular polygon with $n = 10$ edges initially in contact with the surface at one fixed vertex. (b) The compressed shape under a constant, uniaxial (normal) force. Red: the circular sector that best fits the free perimeter. (c) The final shape after removal of the normal force under the constraint of irreversible adhesion.

In AFM, a sharp (several nm) probe is brought in the proximity of the sample surface until the probe-sample distance is so small that interfacial forces between the two become measurable. By raster scanning the probe over the sample while simultaneously adjusting the probe-sample distance accordingly the sample topography to maintain a constant interfacial force, one generates a nanoscopic map of the sample topography. Scan areas may span from several nm^2 to several hundreds of $\mu\mathrm{m}^2$.

In a direction normal to the substrate, spatial resolution is typically better than a nanometre. However, lateral resolution is limited by the sample topographic range and the probe radius (Figure 1).

Since the normal pressure can be adjusted at will during imaging, one can create three-dimensional topographic maps of the upper shell under several constant forces. Our hypothesis is that, from these topographic maps one should be able to determine the mechanical parameters that describe bending and stretching of the shell under deformation.

3. Geometrical preliminaries

In this paper, we consider the deformation of a convex regular polygon with n edges whose vertices (and so the edges) are subjected not to cross an *undeformable* flat surface. We assume that one and only one vertex of the undeformed reference configuration is initially in contact with the flat surface, and we denote this vertex by P_1. The vertices of the polygon are labelled counter-clockwise from P_1 to P_n (Figure 2 a). We further *assume* that the vertex P_1 undergoes no displacement; this assumption is critical to establish the existence and uniqueness of the solution of the governing equations. We minimize the energy associated with the deformation of the convex regular polygon with n edges under two types of constraints: (i) under the action of an applied body force (Figure 2b) and (ii) after the force is removed, under the assumption of irreversible adhesion, i.e. vertexes brought on the rigid surface by the inward pressure in (i) will remain on the surface at force removal (Figure 2c). We consider the elastic energy to have a quadratic dependence on the elongation of the edges as well as the variation of the angle between any pairs of consecutive edges [4]. Furthermore, we assume that the edges are *massless* and can *only stretch*, in the sense that *there is no torsion acting on them*.

A point A in the plane corresponds to a vector in $\mathbb{R}^2$ of the form $A = \binom{x_A}{y_A}$, where $x_A \in \mathbb{R}$ denotes the abscissa of the point and $y_A \in \mathbb{R}$ denotes its ordinate. Let us consider a Cartesian frame for the two-dimensional plane with origin $O = \binom{0}{0}$ and with canonical directions $\vec{e}_1 = \binom{1}{0}$ and $\vec{e}_2 = \binom{0}{1}$.

The position vector associated with the point A is denoted by $\overrightarrow{OA}$; the transpose of a vector $\overrightarrow{OA}$ is denoted by $\overrightarrow{OA}^T = (x_A, y_A)$; the angle between three points A, B and C with vertex at B is either denoted by $\widehat{ABC}$ or by a Greek letter. The Euclidean inner product and the vector product between two vectors $\overrightarrow{OA}$ and $\overrightarrow{OB}$ are respectively denoted by $\overrightarrow{OA} \cdot \overrightarrow{OB} = \overrightarrow{OA}^T \overrightarrow{OB}$ and $\overrightarrow{OA} \times \overrightarrow{OB}$. The Euclidean

norm of $\overrightarrow{OA}$ is denoted $|\overrightarrow{OA}|$. Matrices, apart from the identity matrix $\mathcal{I}$ and the square null matrix $\mathcal{O}$, are denoted by capital Greek letters. Tensors are denoted by boldface capital Latin letters.

Let $n \geq 3$ be an integer number. A regular polygon with n edges is the portion of plane within a non-self intersecting closed broken line, whose n edges have all the same length (cf., e.g. [39]).

4. Formulation and well-posedness of the two-dimensional discrete model

When a vertex P_i of the convex regular polygon with n edges under consideration undergoes the action of an applied body force, we denote by P_i' the new coordinates of the vertex in the plane.

Let $\boldsymbol{F} = (\vec{f}_i)_{i=2}^n \in \mathbb{R}^{2n-2}$ denote the array of applied body forces acting on the polygon, where the vector $\vec{f}_i$ denotes the applied body force acting on the vertex P_i. The application of the force vector $\vec{f}_i$ on the point P_i displaces the position vector $\overrightarrow{OP_i}$ by a vector $\vec{u}_i$, and transforms the vector $\overrightarrow{OP_i}$ into the vector $\overrightarrow{OP_i'}$ via the following relation:

$$\overrightarrow{OP_i'} = \overrightarrow{OP_i} + \vec{u}_i, \quad \text{for each } 2 \leq i \leq n.$$

We denote by ℓ the length of any edge of the undeformed reference configuration of the convex regular polygon with n edges under consideration, namely,

$$\left|\overrightarrow{P_iP_{i+1}}\right| = \ell,$$

where the indices are meant from now on *modulo n*.

Since the point P_1 undergoes, by assumption, no deformation we let $\vec{u}_1 = (0,0)^T$. The stretching energy associated with the displacement

$$\boldsymbol{U} = \begin{pmatrix} \vec{u}_2 \\ \vdots \\ \vec{u}_n \end{pmatrix} \in \mathbb{R}^{2n-2},$$

is computed via Hooke's law (cf., e.g. [40]), i.e.

$$J_s(\boldsymbol{U}) := \frac{k}{4} \sum_{i=2}^{n} \sum_{j \in \{i-1, i+1\}} |\vec{u}_i - \vec{u}_j|^2,$$

where the elastic constant $k > 0$ is associated with the elongation properties of the constitutive material, and the nature of the energy is aptly recalled by the subscript 's'.

The stretching energy $J_s(\boldsymbol{U})$ can equivalently be expressed in matrix form. The matrix associated with the stretching elastic force is a $2n \times (2n-2)$ matrix

$$\Sigma = \frac{1}{2} \begin{pmatrix} -\mathcal{I} & \mathcal{O} & \mathcal{O} & \dots & \mathcal{O} \\ \mathcal{I} & -\mathcal{I} & \mathcal{O} & \dots & \mathcal{O} \\ \vdots & & & \ddots & \\ \mathcal{O} & \dots & \mathcal{O} & \mathcal{I} & -\mathcal{I} \\ \mathcal{O} & \dots & \mathcal{O} & \mathcal{O} & \mathcal{I} \end{pmatrix}.$$

Therefore, the stretching energy $J_s(\boldsymbol{U})$ in matrix form is

$$J_s(\boldsymbol{U}) = k \boldsymbol{U}^T \Sigma^T \Sigma \boldsymbol{U}.$$

The matrix $\Sigma^T \Sigma$ is positive-definite, in the sense that the smallest eigenvalue is greater than zero. To see this, it suffices to observe that the matrix Σ has the same structure as the discrete gradient matrix (cf., e.g. [41]).

The variation of the angle between two consecutive edges is also associated with a change in the energy. From now on, we will refer to this kind of energy as *bending energy*. Denote by $\alpha_i = \widehat{P_{i-1}P_iP_{i+1}}$ the angle between the points P_{i-1}, P_i and P_{i+1} that intersects the interior of the polygon under consideration.

If the action of an applied body forces changes the angle α_i into the angle $\alpha_i' = \widehat{P_{i-1}'P_i'P_{i+1}'}$, the corresponding bending energy is given by

$$\frac{\kappa}{2}|\alpha_i - \alpha_i'|^2,$$

where the elastic constant $\kappa > 0$ is associated with the bending properties of the constitutive material.

If the difference between α_i and α_i' is small, we can approximate $\alpha_i - \alpha_i' \approx \sin(\alpha_i - \alpha_i')$. The latter has the advantage that it can be expressed in terms of a vector product. More specifically, we have:

$$\begin{aligned}\alpha_i - \alpha_i' &\approx \sin(\alpha_i - \alpha_i') = \sin\alpha_i\cos\alpha_i' - \cos\alpha_i\sin\alpha_i' \\ &= \frac{|\overrightarrow{P_iP_{i+1}} \times \overrightarrow{P_{i-1}P_i}|}{|\overrightarrow{P_iP_{i+1}}||\overrightarrow{P_{i-1}P_i}|}\frac{\overrightarrow{P_{i-1}'P_i'} \cdot \overrightarrow{P_i'P_{i+1}'}}{|\overrightarrow{P_i'P_{i+1}'}||\overrightarrow{P_{i-1}'P_i'}|} - \frac{\overrightarrow{P_{i-1}P_i} \cdot \overrightarrow{P_iP_{i+1}}}{|\overrightarrow{P_iP_{i+1}}||\overrightarrow{P_{i-1}P_i}|}\frac{|\overrightarrow{P_i'P_{i+1}'} \times \overrightarrow{P_{i-1}'P_i'}|}{|\overrightarrow{P_i'P_{i+1}'}||\overrightarrow{P_{i-1}'P_i'}|}.\end{aligned}$$

Let us observe that, if the displacement $\boldsymbol{U} = (\vec{u}_i)_{i=2}^n$ is infinitesimal, we have

$$|\overrightarrow{P_{i-1}'P_i'}| \approx |\overrightarrow{P_{i-1}P_i}|.$$

Since

$$\overrightarrow{P_{i-1}'P_i'} = \overrightarrow{OP_i'} - \overrightarrow{OP_{i-1}'} = \overrightarrow{OP_i} + \vec{u}_i - \overrightarrow{OP_{i-1}} - \vec{u}_{i-1} = \overrightarrow{P_{i-1}P_i} + \vec{u}_i - \vec{u}_{i-1},$$

then the properties of the vector product (cf., e.g. [42]) in turn imply:

$$|\overrightarrow{P_i'P_{i+1}'} \times \overrightarrow{P_{i-1}'P_i'}| = |(\overrightarrow{P_iP_{i+1}} + \vec{u}_{i+1} - \vec{u}_i) \times (\overrightarrow{P_{i-1}P_i} + \vec{u}_i - \vec{u}_{i-1})| \approx |\overrightarrow{P_iP_{i+1}} \times \overrightarrow{P_{i-1}P_i}|.$$

Therefore, the angle variation reads

$$\begin{aligned}\alpha_i - \alpha_i' &\approx \frac{|\overrightarrow{P_iP_{i+1}} \times \overrightarrow{P_{i-1}P_i}|}{|\overrightarrow{P_iP_{i+1}}|^2|\overrightarrow{P_{i-1}P_i}|^2}\left(\overrightarrow{P_{i-1}'P_i'} \cdot \overrightarrow{P_i'P_{i+1}'} - \overrightarrow{P_{i-1}P_i} \cdot \overrightarrow{P_iP_{i+1}}\right) \\ &= \frac{|\overrightarrow{P_iP_{i+1}} \times \overrightarrow{P_{i-1}P_i}|}{|\overrightarrow{P_iP_{i+1}}|^2|\overrightarrow{P_{i-1}P_i}|^2}\left((\overrightarrow{P_{i-1}P_i} + \vec{u}_i - \vec{u}_{i-1}) \cdot (\overrightarrow{P_iP_{i+1}} + \vec{u}_{i+1} - \vec{u}_i) - \overrightarrow{P_{i-1}P_i} \cdot \overrightarrow{P_iP_{i+1}}\right) \\ &\approx \frac{|\overrightarrow{P_iP_{i+1}} \times \overrightarrow{P_{i-1}P_i}|}{|\overrightarrow{P_iP_{i+1}}|^2|\overrightarrow{P_{i-1}P_i}|^2}\left(\overrightarrow{P_{i-1}P_i} \cdot (\vec{u}_{i+1} - \vec{u}_i) + \overrightarrow{P_iP_{i+1}} \cdot (\vec{u}_i - \vec{u}_{i-1})\right) \\ &= \frac{|\overrightarrow{P_iP_{i+1}} \times \overrightarrow{P_{i-1}P_i}|}{|\overrightarrow{P_iP_{i+1}}|^2|\overrightarrow{P_{i-1}P_i}|^2}\left(\overrightarrow{P_{i-1}P_i} \cdot \vec{u}_{i+1} + (\overrightarrow{P_iP_{i+1}} - \overrightarrow{P_{i-1}P_i}) \cdot \vec{u}_i - \overrightarrow{P_iP_{i+1}} \cdot \vec{u}_{i-1}\right).\end{aligned}$$

Letting $C := \frac{|\overrightarrow{P_iP_{i+1}} \times \overrightarrow{P_{i-1}P_i}|}{|\overrightarrow{P_iP_{i+1}}|^2|\overrightarrow{P_{i-1}P_i}|^2}$ and observing that this quantity is independent of the index i, we can express the total bending energy in terms of the vertices displacements:

$$J_b(\boldsymbol{U}) = \frac{\kappa C^2}{2}\sum_{i=2}^{n}\left|\overrightarrow{P_{i-1}P_i} \cdot \vec{u}_{i+1} + (\overrightarrow{P_iP_{i+1}} - \overrightarrow{P_{i-1}P_i}) \cdot \vec{u}_i - \overrightarrow{P_iP_{i+1}} \cdot \vec{u}_{i-1}\right|^2.$$

The bending energy $J_b(\boldsymbol{U})$ can equivalently be expressed in matrix form. The matrix associated with the bending elastic force is a $n \times (2n-2)$ matrix:

$$\Theta = \begin{pmatrix} (\overrightarrow{P_2P_3} - \overrightarrow{P_1P_2})^T & \overrightarrow{P_1P_2}^T & 0 & \dots & 0 \\ \overrightarrow{P_3P_4}^T & (\overrightarrow{P_3P_4} - \overrightarrow{P_2P_3})^T & \overrightarrow{P_2P_3}^T & \dots & 0 \\ \vdots & & & \ddots & \\ 0 & \dots & 0 & (\overrightarrow{P_{n-1}P_n} - \overrightarrow{P_{n-2}P_{n-1}})^T & \overrightarrow{P_{n-2}P_{n-1}}^T \\ 0 & \dots & 0 & \overrightarrow{P_nP_1}^T & (\overrightarrow{P_nP_1} - \overrightarrow{P_{n-1}P_n})^T \end{pmatrix}.$$

Therefore, the bending energy $J_b(\boldsymbol{U})$ in matrix form is

$$J_b(\boldsymbol{U}) = \frac{\kappa C^2}{2} \boldsymbol{U}^T \Theta^T \Theta \boldsymbol{U},$$

where the nature of the energy is aptly recalled by the subscript 'b'.

The matrix $\Theta^T\Theta$ is nonnegative-definite, in the sense that the smallest eigenvalue is greater or equal than zero. The total elastic energy associated with the displacement tensor $\boldsymbol{U}$ thus takes the following form:

$$J(\boldsymbol{U}) = J_s(\boldsymbol{U}) + J_b(\boldsymbol{U}) = \boldsymbol{U}^T \left(k\Sigma^T\Sigma + \frac{\kappa C^2}{2}\Theta^T\Theta \right) \boldsymbol{U},$$

so that the total energy matrix is positive-definite, being $\Sigma^T\Sigma$ positive-definite. This makes the total elastic energy a strictly convex quadratic functional.

The search for an equilibrium position for the deformed polygon amounts to minimizing the corresponding total elastic energy. In view of the geometrical constraint according to which the vertices do not have to cross the given flat surface, the admissible displacement fields are to be sought in the following set:

$$\mathcal{U} := \left\{ \boldsymbol{V} = (\vec{v}_i)_{i=2}^n \in \mathbb{R}^{2n-2}; \vec{v}_i = \begin{pmatrix} v_{i,1} \\ v_{i,2} \end{pmatrix} \text{ and } (\overrightarrow{OP_i} + \vec{v}_i) \cdot \vec{e}_2 \geq 0 \text{ for all } 2 \leq i \leq n \right\}.$$

It is straightforward to observe that the set $\mathcal{U}$ is non-empty (as $\boldsymbol{V} = \boldsymbol{0} \in \mathcal{U}$), closed and convex.

Therefore, the latter together with the fact that the total elastic energy functional is strictly convex, imply that the quadratic minimization problem

$$\inf_{\boldsymbol{V} \in \mathcal{U}} (J(\boldsymbol{V}) - \boldsymbol{F}^T \boldsymbol{V})$$

admits a unique minimizer (cf., e.g. [43]). Finding the solution for this minimization problem is equivalent to finding a tensor $\boldsymbol{U}$ that solves the following variational inequalities [44]:

$$\left(\left(k\Sigma^T\Sigma + \frac{\kappa C^2}{2}\Theta^T\Theta \right) \boldsymbol{U} \right) \cdot (\boldsymbol{V} - \boldsymbol{U}) \geq \frac{1}{2} \boldsymbol{F} \cdot (\boldsymbol{V} - \boldsymbol{U}), \quad \text{for all } \boldsymbol{V} \in \mathcal{U}.$$

5. Numerical experiments. Part I: Analysis of the deformation under the action of an applied body force

The first numerical experiment we conduct on the proposed model is classical and amounts to finding the position of the deformed reference configuration of the convex regular polygon undergoing the

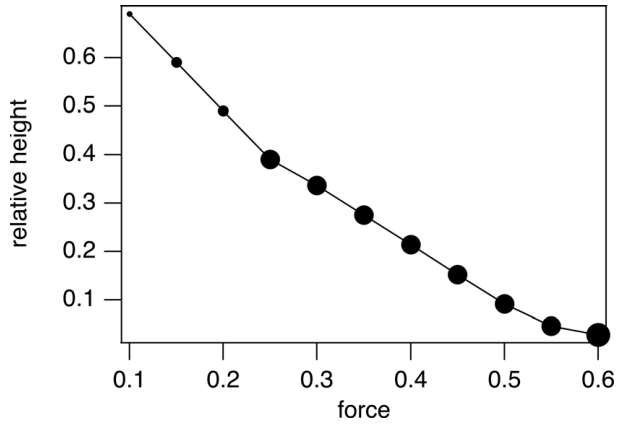

Figure 3. Changes in height above the base line, relative to the initial value as the force per vertex is increased. Different marker sizes are associated with different numbers of contact vertices.

action of an applied body force which acts on each vertex with the same magnitude. This distributed applied force models the downward pressure that an AFM probe, which is comparable in size with the virus will exert.

The numerical implementation for the problem under consideration is carried out by resorting to the primal–dual active set method (cf., e.g. [45]). We consider different instances of the array $\boldsymbol{F} = (\vec{f}_i)_{i=2}^{n}$ of applied body forces whose tangential component is zero and whose transverse component is directed downwards, as well as a varying number n of vertices.

Figure 2(b) shows the shape of a regular decagon under directional pressure for the values $k = \kappa = 1.0$, and $f = 0.25$ in reduced units. For this specific load magnitude, half of the vertices are on the surface and half are free. The free vertices align with a good approximation on a circle. The radius of the circle that best approximates the polygonal segment formed of free vertices is 1.9 times the radius of the circle in which the initial regular polygon was inscribed. The top of the deformed polygon is at 0.41 from the initial, unperturbed value. We can now predict how the apparent height above the surface changes as a function of the AFM imaging force. The apparent height is an accurately measurable quantity. Figure 3 shows the result of such a prediction for the same decagon. The apparent height above the surface decreases smoothly with the applied pressure. This result is consistent with experimental observations obtained from AFM on the brome mosaic virus [5]. However, breaks in the slope due to discrete changes in the number of sides laying flat on the base line are noticeable. While the apparent height varies continuously, the number of surface contacts and hence the surface adhesion does not (Figure 4). Considering that the imaged structure is the result of the balancing act between adhesive, pressure, and elastic forces, the latter observation predicts that the number of contacts could be discreetly varied by imaging at various probe pressures. On hydrophobic surfaces, much like the substrates used in AFM imaging, adhesion is usually strong and irreversible. Thus, by imaging at low pressures after an initial higher pressure scan, the contact area can be deduced from the height and shape of the free surface as the particle relaxes. In other words, for a relaxed polygon (no pressure) with a given partial contact length the shape and the height above the base line should vary discretely, as a function of the number of contacts with the baseline.

By imaging at high force, and then at low force, and comparing with a model based on the one presented here, one should be able, for the first time, to determine the virus-surface contact area that corresponds to a certain applied force. This is why, we have considered useful to extend our numerical approach and calculate the shape of the polygon, as a function of the number of contact vertices (and thus of the initial imaging force) once the external force has been turned off (Figure 2c).

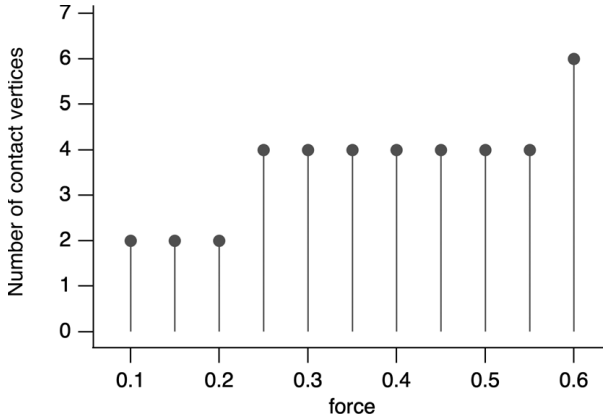

Figure 4. Changes in the number of points in contact with the flat surface as applied force is increased for a decagon.

Table 1. Ratio of upper polygon average radius (R) and initial, undeformed radius (R_0) as a function of the number of baseline vertices.

Number of base line vertices	3	5	7
R/R_0	0.99	1.05	1.04

6. Numerical experiments. Part II: search for a new equilibrium position for the polygon and correlation with the continuous model

In the second experiment, we *assume* that the vertices of the polygon which engage contact with the surface as a result of the application of the applied body force under consideration (cf. Section 5) remain in contact with the surface when the applied body force ceases to act. This corresponds to the case where the AFM cantilever pushing the ring downwards is lifted and a certain adhesion force acts on the part of the elastic structure that engaged contact with the flat surface.

As a result, the vertices which do not engage contact with the surface tend to re-organize themselves in a way that minimizes the elastic energy; the points in contact with the surface are only allowed to slide horizontally on the surface. The latter assumption is based on the observation that the activation energy for surface diffusion of adsorbed molecules is usually at least an order of magnitude smaller than the adsorption energy [46]. Thus lateral sliding is much more likely to occur than desorption.

Because of its accurate measurability and practical interest, we study the root-mean-square fitted average radius of the free sector (vertices that do not engage with the surface) after the equilibrium restoration of the elastic polygon as a function of the number of contact points with the base line (or, equivalent, as a function of the initial compression described in the previous section). We then verify the genuineness of the proposed discrete model via a set of numerical experiments, where the number of vertices vary. The expectation is that the relaxed shape will tend towards a circular sector that minimizes the line tension.

Table 1 shows the dependence of the r.m.s. average radius of curvature of the free portion of the decagon on the number of base line contacts. The changes in the average curvature of the polygon as the number of contact vertices is increased in this example are small, but it is reasonable to assume that they will be measurable if $\sim 10^2$ data points collected during topographic mapping will be used for fitting. As mentioned before, the spatial resolution in the normal direction to the base line is better than 0.5 nm, while the radius of a virus particle is typically 30–100 nm.

Finally, we consider the case where the same total vertical body force is applied, and we let the number of vertices increase. The final polygonal shape should converge to the one expected from

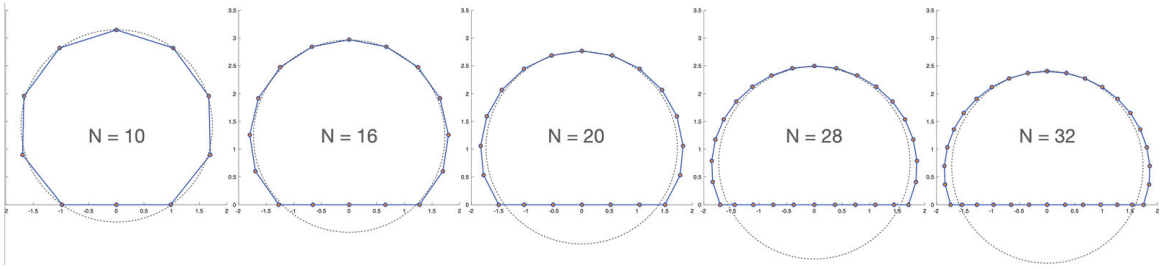

Figure 5. Increasing the number of total vertices while keeping all other parameters constant leads to a shape that does not change anymore at higher number of vertices. The dotted line circle corresponds to the circle circumscribing the initial regular polygon and is provided as a reference.

a continuum approach, with a circular free perimeter, a fixed contact angle and height at the top. Figure 5 shows the result of such a comparison.

Beyond $N \approx 25$ the shape does not change anymore. At this point, a continuum description will be adequate. The dotted line circle in Figure 5 corresponds to the circle that circumscribes the initial, regular polyhedron, added to the polygonal shape in a way that superposes the apex point of the circle and the polygon and preserves the left-right symmetry. Below the continuum threshold, there are some variations of the polygonal shape with respect to the circumscribing circle, but they are rather minor in the vicinity of the apex point. However, the apex point height varies significantly below the continuum threshold. The practical outcome of this observation is that the AFM measurement of the top part of the virus, which is very accurate, could be used in fitting it at every map point with a spherical shell. It is not unreasonable to hypothesize that, from the radius and the center of curvature for that shell one could deduce the elastic constants of the virus particle at an unprecedented level of accuracy.

7. Conclusion

In conclusion, we present a simple model for virus deformation under AFM imaging conditions. The model includes discrete units and deformation modes, adhesion to a substrate, and unidirectional loading forces. We show that numerical solutions based on the model provide a solution uniquely associated to a set of parameters. As a direct application of our analysis, we propose a novel method of using the AFM topographic mapping under different imaging force loads that should lead to determinations of the contact area and elastic constants. The advantages of this approach with respect to state-of-the art elastic deformation studies will be: (1) high throughput, because many viruses can be imaged at the same time, and (2) accuracy, because the resolution of the topographic mapping is very high (sub-nm) in a direction normal to the substrate, even at physiological conditions.

In the forthcoming paper [29], where we study a three-dimensional model governing the deformation of viral capsids, we will compare the numerical results with experimental ones.

Disclosure statement

No potential conflict of interest was reported by the author(s).

Funding

We gratefully acknowledge support by the Army Research Office, under award W911NF-17-1-0329 and by the National Science Foundation, under award CBET 1803440 and 1808027 (to BD). We acknowledge the Center for Bioanalytical Metrology (CBM), an NSF Industry-University Cooperative Research Center, for providing funding under grant NSF IIP 1916645. This work was partly supported by the Research Fund of Indiana University.

References

[1] Sloan ED. Fundamental principles and applications of natural gas hydrates. Nature. 2003 Nov;426(6964):353–359. DOI:10.1038/nature02135

[2] Greber UF. How cells tune viral mechanics–insights from biophysical measurements of influenza virus. Biophys J. 2014 Jun;106(11):2317–2321. DOI:10.1016/j.bpj.2014.04.025

[3] Guerra P, Valbuena A, Querol-Audí J, et al. Structural basis for biologically relevant mechanical stiffening of a virus capsid by cavity-creating or spacefilling mutations. Sci Rep. 2017 Dec;7(1):4101. DOI:10.1038/s41598-017-04345-w

[4] Zeng C, Hernando-Pérez M, Dragnea B, et al. Contact mechanics of a small icosahedral virus. Phys Rev Lett. 2017 Jul;119(3):Article ID 038102.DOI:10.1103/PhysRevLett.119.038102

[5] Zeng C, Scott L, Malyutin A, et al. Virus mechanics under molecular crowding. J Phys Chem B. 2021 Feb;125(7):1790–1798. DOI:10.1021/acs.jpcb.0c10947

[6] Prevelige PE, Thomas D, KING J. Nucleation and growth phases in the polymerization of coat and scaffolding subunits into icosahedral procapsid shells. Biophys J. 1993 Mar;64(3):824–835.

[7] Zlotnick A, Johnson JM, Wingfield PW, et al. A theoretical model successfully identifies features of hepatitis B virus capsid assembly. Biochemistry. 1999 Nov;38(44):14644–14652.

[8] Dragnea B. Watching a virus grow. 2019 Nov. Available from: https://www.pnas.org/content/116/45/22420.short?rss=1.

[9] Zlotnick A. Distinguishing reversible from irreversible virus capsid assembly. J Mol Biol. 2007 Feb;366(1):14–18.

[10] Aggarwal A, Rudnick J, Bruinsma RF, et al. Elasticity theory of macromolecular aggregates. Phys Rev Lett. 2012 Oct;109(14):Article ID 148102. DOI:10.1103/PhysRevLett.109.148102

[11] Zandi R, Reguera D. Mechanical properties of viral capsids. Phys Rev E. 2005 Aug;72(2):Article ID 021917.DOI:10.1103/PhysRevE.72.021917

[12] Ivanovska IL, de Pablo PJ, Ibarra B, et al. Bacteriophage capsids: tough nanoshells with complex elastic properties. Proc Natl Acad Sci. 2004 May;101(20):7600–7605. DOI:10.1073/pnas.0308198101

[13] Michel JP, Ivanovska IL, Gibbons MM, et al. Nanoindentation studies of full and empty viral capsids and the effects of capsid protein mutations on elasticity and strength. Proc Natl Acad Sci. 2006 Apr;103(16):6184–6189. DOI:10.1073/pnas.0601744103

[14] Roos WH. How to perform a nanoindentation experiment on a virus. Methods Mol Biol. 2011 Jan;783:251–264. DOI:10.1007/978-1-61779-282-3_14

[15] Thompson WC, Cattani AJ, Lee O, et al. A laboratory model for virus particle nanoindentation. Biophysicist. 2020 Jan;1(2):DOI:10.35459/tbp.2019.000106

[16] Bruinsma RF, Klug WS. Physics of viral shells. Annu Rev Condens Matter Phys. 2015 Mar;6(1):245–268. DOI:10.1146/annurev-conmatphys-031214-014325

[17] Gibbons MM, Klug WS. Mechanical modeling of viral capsids. J Mater Sci. 2007 Jul;42(21):8995–9004. DOI:10.1007/s10853-007-1741-4

[18] Arkhipov A, Roos WH, Wuite GJL, et al. Elucidating the mechanism behind irreversible deformation of viral capsids. Biophys J. 2009 Oct;97(7):2061–2069. DOI:10.1016/j.bpj.2009.07.039

[19] Krishnamani V, Globisch C, Peter C, et al. Breaking a virus: identifying molecular level failure modes of a viral capsid by multiscale modeling. Eur Phys J Spec Top. 2016 Jul;1–18. DOI:10.1140/epjst/e2016-60141-2

[20] Mannige RV, Brooks CL. Geometric considerations in virus capsid size specificity, auxiliary requirements, and buckling. Proc Natl Acad Sci. 2009 May;106(21):8531–8536. DOI:10.1073/pnas.0811517106

[21] Vliegenthart GA, Gompper G. Mechanical deformation of spherical viruses with icosahedral symmetry. Biophys J. 2006 Aug;91(3):834–841. DOI:10.1529/biophysj.106.081422

[22] Ciarlet PG, Piersanti P. Obstacle problems for Koiter's shells. Math Mech Solids. 2019;24:3061–3079.

[23] Ciarlet PG, Piersanti P. A confinement problem for a linearly elastic Koiter's shell. C R Math. 2019;357:221–230.

[24] Ciarlet PG, Mardare C, Piersanti P. Un problème de confinement pour une coque membranaire linéairement élastique de type elliptique. C R Math. 2018;356(10):1040–1051.

[25] Ciarlet PG, Mardare C, Piersanti P. An obstacle problem for elliptic membrane shells. Math Mech Solids. 2019;24(5):1503–1529.

[26] Piersanti P. On the improved interior regularity of the solution of a fourth order elliptic problem modelling the displacement of a linearly elastic shallow shell subject to an obstacle. Asymptot Anal. 2021;127:1–21.

[27] Piersanti P, Shen X. Numerical methods for static shallow shells lying over an obstacle. Numer Algorithms. 2020;85623–652.

[28] Piersanti P. A time-dependent obstacle problem in linearised elasticity. Nonlinear Anal. 2020;192:Article ID 111660.

[29] Piersanti P, White K, Dragnea B, et al. A three-dimensional discrete model for approximating the deformation of a viral capsid subjected to lying over a flat surface. In preparation. Preprint arxiv. https://arxiv.org/abs/2202.05625

[30] Baclayon M, Wuite GJL, Roos WH. Imaging and manipulation of single viruses by atomic force microscopy. Soft Matter. 2010;6(21):5273–5285. DOI:10.1039/b923992h

[31] Calo A, Eleta-Lopez A, Ondarcuhu T, et al. Nanoscale wetting of single viruses. Molecules. 2021 Aug;26(17):5184.DOI:10.3390/molecules26175184
[32] Cartagena A, Hernando-Pérez M, Carrascosa JL, et al. Mapping in vitro local material properties of intact and disrupted virions at high resolution using multi-harmonic atomic force microscopy. Nanoscale. 2013;5(11):4729. DOI:10.1039/c3nr34088k
[33] Kuznetsov YG, McPherson A. Atomic force microscopy investigation of viruses. Methods Mol Biol. 2011 Apr;736(4):171–195.
[34] Castellanos M, Pérez R, Carrasco C, et al. Mechanical elasticity as a physical signature of conformational dynamics in a virus particle. Proc Natl Acad Sci. 2012 Jul;109(30):12028–12033. DOI:10.1073/pnas.1207437109
[35] Kononova O, Snijder J, Brasch M, et al. Structural transitions and energy landscape for cowpea chlorotic mottle virus capsid mechanics from nanomanipulation in vitro and in silico. Biophys J. 2013 Oct;105(8):1893–1903. DOI:10.1016/j.bpj.2013.08.032
[36] Mateu MG. Mechanical properties of viruses analyzed by atomic force microscopy: a virological perspective. Virus Res. 2012 Sep;168(1–2):1–22. DOI:10.1016/j.virusres.2012.06.008
[37] Pang H-B, Hevroni L, Kol N, et al. Virion stiffness regulates immature HIV-1 entry. Retrovirology. 2013 Jan;10:4.DOI:10.1186/1742-4690-10-4
[38] Snijder J, Reddy VS, May ER, et al. Integrin and defensin modulate the mechanical properties of adenovirus. J Virol. 2013 Mar;87(5):2756–2766. DOI:10.1128/JVI.02516-12
[39] Kiselev AP. Geometry. Book I. Planimetry. Sumizdat; 2006.
[40] Temam R, Miranville A. Mathematical modeling in continuum mechanics. 2nd ed. Cambridge: Cambridge University Press; 2005.
[41] Quarteroni A, Saleri F, Gervasio P. Scientific computing with MATLAB and octave. Berlin: Springer-Verlag; 2010. (Texts in computational science and engineering; vol. 2).
[42] Strang G. Linear algebra and its applications. 2nd ed. New York: Academic Press; 1980.
[43] Ekeland I, Temam R. Convex analysis and variational problems. english ed. Translated from the French. Philadelphia (PA): Society for Industrial and Applied Mathematics (SIAM); 1999. (Classics in applied mathematics; vol. 28).
[44] Duvaut G, Lions J-L. Inequalities in mechanics and physics. Berlin: Springer; 1976.
[45] Sun W, Yuan Y-X. Optimization theory and methods: nonlinear programming. New York: Springer; 2006. (Springer optimization and its applications; vol. 1).
[46] Somorjai GA. Introduction to surface chemistry and catalysis. New York: John Wiley & Sons; 1994.